The Astrophysical Journal Letters, 963:L38 (12pp), 2024 March 10 https://doi.org/10.3847/2041-8213/ad292f

Unveiling Luminous Lyα Emitters at $z \approx 6$ through JWST/NIRCam Imaging in the COSMOS Field

Yuanhang Ning[1], Zheng Cai[1], Xiaojing Lin[1], Zhen-Ya Zheng[2], Xiaotong Feng[3,4], Mingyu Li[1], Qiong Li[5], Daniele Spinoso[1], Yunjing Wu[1], and Haibin Zhang[1]
[1] Department of Astronomy, Tsinghua University, Beijing 100084, People's Republic of China; ningyhphy@mail.tsinghua.edu.cn, zcai@mail.tsinghua.edu.cn
[2] CAS Key Laboratory for Research in Galaxies and Cosmology, Shanghai Astronomical Observatory, Shanghai 200030, People's Republic of China
[3] Department of Astronomy, School of Physics, Peking University, Beijing 100871, People's Republic of China
[4] Kavli Institute for Astronomy and Astrophysics, Peking University, Beijing 100871, People's Republic of China
[5] Jodrell Bank Centre for Astrophysics, University of Manchester, Oxford Road, Manchester M13 9PL, UK
Received 2023 December 8; revised 2024 February 5; accepted 2024 February 13; published 2024 March 5

Abstract

We study a sample of 14 spectroscopically confirmed Lyα emitters (LAEs) in the late era of reionization (at redshift $z \approx 6$) based on the JWST/NIRCam imaging data set. These LAEs with high Lyα luminosity of $L(\mathrm{Ly}\alpha) \sim 10^{42.4}$–$10^{43.4}$ erg s^{-1} have been covered by the (ongoing) COSMOS-Web survey over 0.28 deg^2 in four NIRCam bands (F115W, F150W, F277W, and F444W). With JWST/NIRCam imaging, we determine the UV continua with M_{UV} ranging from -20.5 to -18.5 mag. The UV slopes have a median value of $\beta \approx -2.35$, and the steepest slopes can reach $\beta < -3$. Under the excellent spatial resolution of JWST, we identify three objects in the sample as potential merging/interacting systems. The 14 LAEs (and their components) are compact in morphology, residing substantially below the mass–size relation of high-z galaxies. We further investigate their physical properties, including the stellar mass (M_*) and star formation rates (SFRs). Most of the LAEs lie on the SFR–M_* main-sequence relation, while two of them, featured as "little red dots," likely host active galactic nuclei (AGNs), implying a $\sim$10% AGN fraction. Moreover, we reveal that a new correlation may exist between Lyα equivalent width and the offset between Lyα and UV emission ($\Delta d_{\mathrm{Ly}\alpha}$), with a median $\Delta d_{\mathrm{Ly}\alpha} \sim 1$ kpc. This could be explained by the Lyα radiative transfer process in both the interstellar medium and circumgalactic medium. The results usher in a new era of detailed analysis on high-z LAEs with the JWST capability.

Unified Astronomy Thesaurus concepts: High-redshift galaxies (734); Lyman-alpha galaxies (978); Galaxy properties (615); Galaxy mergers (608); Active galactic nuclei (16); Reionization (1383)

1. Introduction

Thanks to the James Webb Space Telescope (JWST; Gardner et al. 2006), the exploration of high-redshift (high-z) galaxies has recently extended to $z \gtrsim 9$, a highly neutral universe during the epoch of reionization (e.g., Castellano et al. 2022; Treu et al. 2022; Adams et al. 2023; Bradley et al. 2023; Donnan et al. 2023; Franco et al. 2023; Furtak et al. 2023). Previous works can only use Hubble Space Telescope (HST) to study $z \gtrsim 6$ galaxies in detail with both relatively high resolution and sensitivity (e.g., Finkelstein et al. 2012; Jiang et al. 2013b, 2013a; Bouwens et al. 2014; Schmidt et al. 2016; Tilvi et al. 2016). Such space observations usually provide faint samples of high-z objects in a small area.

More luminous galaxies may have complex structures such as Lyα blobs (e.g., Ouchi et al. 2013; Sobral et al. 2019; Zhang et al. 2020). They are thus an ideal laboratory to study formation, interaction, and evolution of galaxies. Currently, only large ground-based surveys can help us find most luminous galaxies. With faint Lyman break galaxies (LBGs) mostly found by HST (e.g., Yan et al. 2012; Oesch et al. 2014; Infante et al. 2015; Laporte et al. 2015; McLeod et al. 2016), a large number of high-z bright LBGs are selected by the dropout technique from large-area ground-based observations (e.g., Curtis-Lake et al. 2012; Laporte et al. 2012; Ono et al. 2018). The narrowband (NB; or Lyα) technique used by large-area ground-based observations provides a complementary method to find high-z galaxies that are relatively luminous Lyα emitters (LAEs; e.g., Kashikawa et al. 2006; Hu et al. 2010; Kashikawa et al. 2011; Jiang et al. 2017; Zheng et al. 2017; Taylor et al. 2020).

The high-z galaxies (e.g., the LBGs and LAEs) have been analyzed based on HST (e.g., Taniguchi et al. 2009; Jiang et al. 2013b, 2013a; Paulino-Afonso et al. 2018; Jiang et al. 2020) and Spitzer observations (e.g., Egami et al. 2005; Huang et al. 2011; Labbé et al. 2013; Ashby et al. 2015; Bradač 2020; Strait et al. 2020; Whitler et al. 2023). However, their physical properties have not been well constrained. For example, Spitzer covers the rest-frame optical bands for the high-z galaxies, but its low resolution makes photometric measurements tentative for the distant small objects. The advent of JWST is solving such problems with its transformative capabilities. Especially, the recently ongoing JWST Cycle 1 program COSMOS-Web (GO-1727; Kartaltepe et al. 2021; Casey et al. 2023) will contribute the largest JWST imaging survey area and cover a number of luminous high-z galaxies.

We have carried out a spectroscopic survey to build a large and homogeneous confirmed sample of high-z galaxies (Jiang et al. 2017). Besides constraining cosmic reionization using LAEs at $z \approx 5.7$ and 6.6 (Ning et al. 2020, 2022), we also aim to study their galaxy properties in detail. As the survey is designed to select high-z galaxies from the famous fields, many of them could be covered by JWST observations, including the above-mentioned COSMOS-Web. The multiple JWST/NIRCam bands

will reveal their individual properties on global and spatially resolved scales. Currently, the COSMOS-Web imaging survey has covered galaxies at $z \sim 6$ that are spectroscopically confirmed by our M2FS survey. In this work, we focus on the properties of the 14 spectroscopically confirmed luminous LAEs at $z \approx 5.7$ based on JWST imaging data in the four NIRCam bands (F115W, F150W, F277W, and F444W).

The paper has the following layout. In Section 2, we briefly describe the sample of luminous LAEs at $z \approx 5.7$, COSMOS-Web NIRCam imaging observations, data reduction, and photometry. We present the results of a variety of properties of the LAE sample in Section 3. We give further discussions in Section 4. We summarize our paper in Section 5. Throughout the paper, we use a standard flat cosmology with $H_0 = 70\,\mathrm{km\,s^{-1}\,Mpc^{-1}}$, $\Omega_m = 0.3$ and $\Omega_\Lambda = 0.7$. All magnitudes refer to the AB system.

2. Sample and Data

In this section, we describe our sample of LAEs at $z \approx 5.7$, JWST/NIRCam imaging observations of the COSMOS-Web program, imaging data reduction, and photometry. We list the observational information of the sample in Table 1.

2.1. Sample of LAEs at z ≈5.7

To build a large and homogeneous sample of high-z galaxies (LBGs at $z \sim 6$ and LAEs at $z \approx 5.7$ and 6.6), we have carried out a spectroscopic survey with a total sky coverage of $\sim$2 deg^2. As designed by our survey, the observed galaxy candidates are selected from Subaru/Suprime broadband and NB images in several well-studied fields, including the Subaru XMM-Newton Deep Survey (SXDS), the Extended Chandra Deep Field South (ECDFS), A370, COSMOS, and SSA22. The utilized instrument in this survey is the fiber-fed, multiobject spectrograph Michigan/Magellan Fiber System (M2FS; Mateo et al. 2012) on the 6.5 m Magellan Clay telescope. In the five fields, we have identified 260 LAEs at $z \approx 5.7$, which by far constitutes the largest spectroscopically confirmed sample of LAEs at this redshift (Ning et al. 2020). In COSMOS, we confirm 52 LAEs at $z \approx 5.7$ from 158 observed candidates. In this work, we focus on 14 LAEs therein that have been covered by the COSMOS-Web JWST/NIRCam imaging observations.

We show the positions of our confirmed LAEs embedded within the COSMOS-Web map of tiling visits in Figure 1(a). Among the 18 LAEs covered by COSMOS-Web observations, we do not include four LAEs in the sample. The reason is that three of them (z6lae-089, z6lae-110, and z6lae-119) are not detected in both F115W and F150W images (before the point-spread function (PSF) matching to F444W; see Section 2.3), while the other one is located in the tile but with unfinished observations. Hence, we have 14 LAEs in our final sample. Note that in the left-hand region, there are only two LAEs from our sample. This is because two M2FS pointings, COSMOS1 and COSMOS3, suffered serious alignment problems as mentioned in Ning et al. (2020). The number density of confirmed LAEs is relatively low in the regions. In Figure 1(b), we plot how the 14 LAEs distribute in the redshift–luminosity space in the lower panel and the number distribution in the upper panel. We can see that the 14 LAEs at $z \approx 5.7$ cover a range of Lyα luminosity over an order of magnitude, which indicates that our sample is representative in terms of Lyα luminosity to study properties of LAEs at this redshift slice.

2.2. COSMOS-Web Imaging Data

Our LAE sample has been covered by the ongoing JWST Cycle 1 program COSMOS-Web (GO-1727; Kartaltepe et al. 2021; Casey et al. 2023) with quick public data release. The COSMOS-Web survey aims to observe a contiguous central area of 0.54 deg^2 in the COSMOS field. It carries out NIRCam imaging observations in four broad bands, including F115W and F150W in the short wavelength (SW) and F277W and F444W in the long wavelength (LW). COSMOS-Web also has a parallel MIRI imaging in the F770W band, which covers a noncontiguous, smaller area of 0.19 deg^2. The whole COSMOS-Web program has 152 separate visits arranged in a 19×8 grid. After the first half of observations, the 14 LAEs in our sample are located in 10 mosaic tiles (Figure 1(a)) whose exposure times in all four bands have reached the designed time of 1031 s. We retrieve the uncalibrated NIRCam imaging data from the Mikulski Archive for Space Telescopes (MAST) Archive at the Space Telescope Science Institute. The specific observations can be accessed via DOI: 10.17909/vvwq-8284.

2.3. Data Reduction and Photometry

We reduce the NIRCam imaging data with the standard JWST pipeline (v1.7.2; Bushouse et al. 2022) up to stage 2 using the reference files "jwst _ 1046.pmap." Then, we use the `Grizli`[6] reduction pipeline to process the output images. `Grizli` mitigates 1/f noises and masks the "snowball" artifacts from cosmic rays (Rigby et al. 2023). It further converts the world coordinate system (WCS) information in the headers to the SIP format for each exposure so that images can be drizzled and combined with Astrodrizzle.[7] For the SW and LW images, the WCS of final mosaics are registered based on the catalogs of DESI Legacy Imaging Surveys Data Release 9, and the pixel scale is resampled to 0.″03 with pixfrac = 0.8. We also subtract an additional background on the final mosaics. Figure 1(c) shows the thumbnail images for our sample of LAEs at $z \approx 5.7$ in the four JWST/NIRCam bands.

We run `SExtractor` (Bertin & Arnouts 1996) to detect the sources and measure the flux in the images in all four JWST/NIRCam bands. As the original target positions are given by the NB data (Lyα centroid), we first match the output catalogs to the targets within a distance tolerance of 0.″3. For each target, we select the band with the highest signal-to-noise ratio (S/N) to feed the detection image. Usually, we adopt the F277W or F444W (boosted by Hα emission) band for most of sources; otherwise, we adopt the SW bands for the multiple components in the merging/interacting systems, z6lae-072 and z6lae-137. We then rerun `SExtractor` in the dual image mode to perform photometry with the corresponding detection images. In this procedure, we create an empirical PSF by coadding at least 100 bright (not saturated) stars for each band and carry out PSF matching to the F444W band. Then, we adopt an aperture with a radius of 0.″15 in each measurement image. The aperture correction is calculated from the empirical PSF in the F444W images. For those containing double components, we adopt the original image for each band in case of source blending and perform photometry using an aperture with a diameter of the distance between the two components. We also improve the photometric measurements by performing

[6] https://github.com/gbrammer/grizli
[7] https://drizzlepac.readthedocs.io/en/latest/astrodrizzle.html

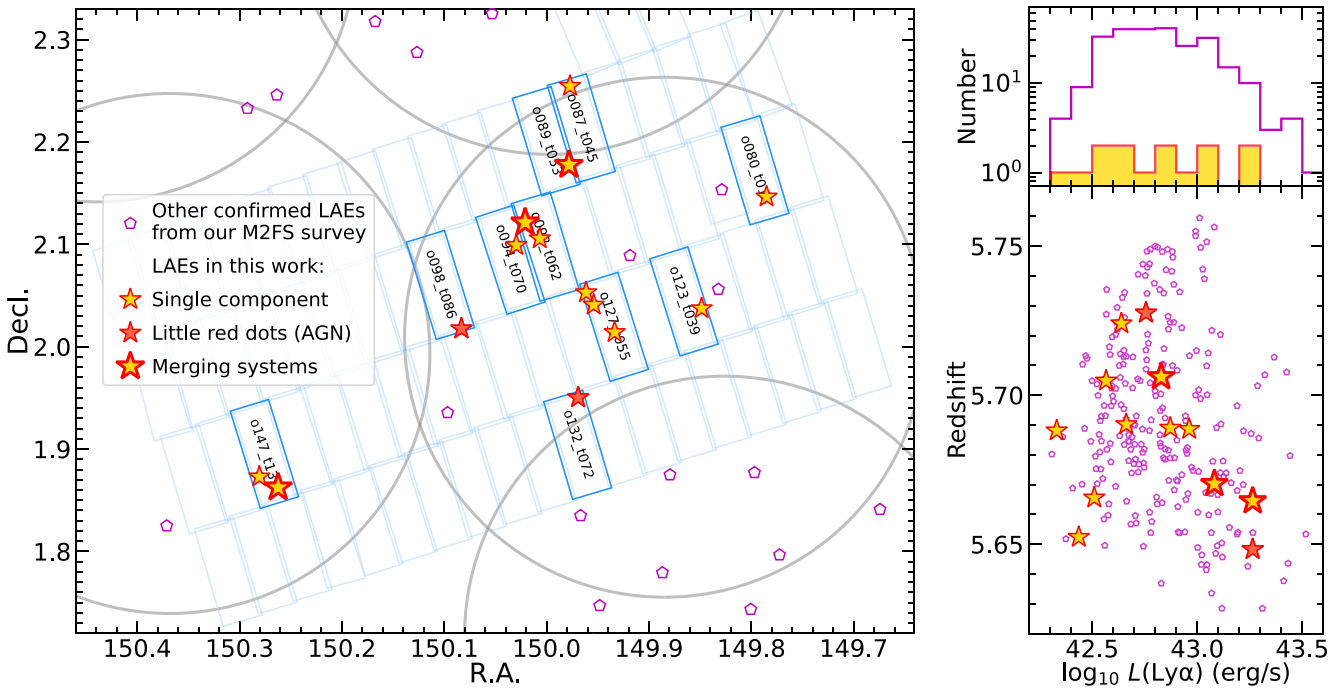

(a) (b)

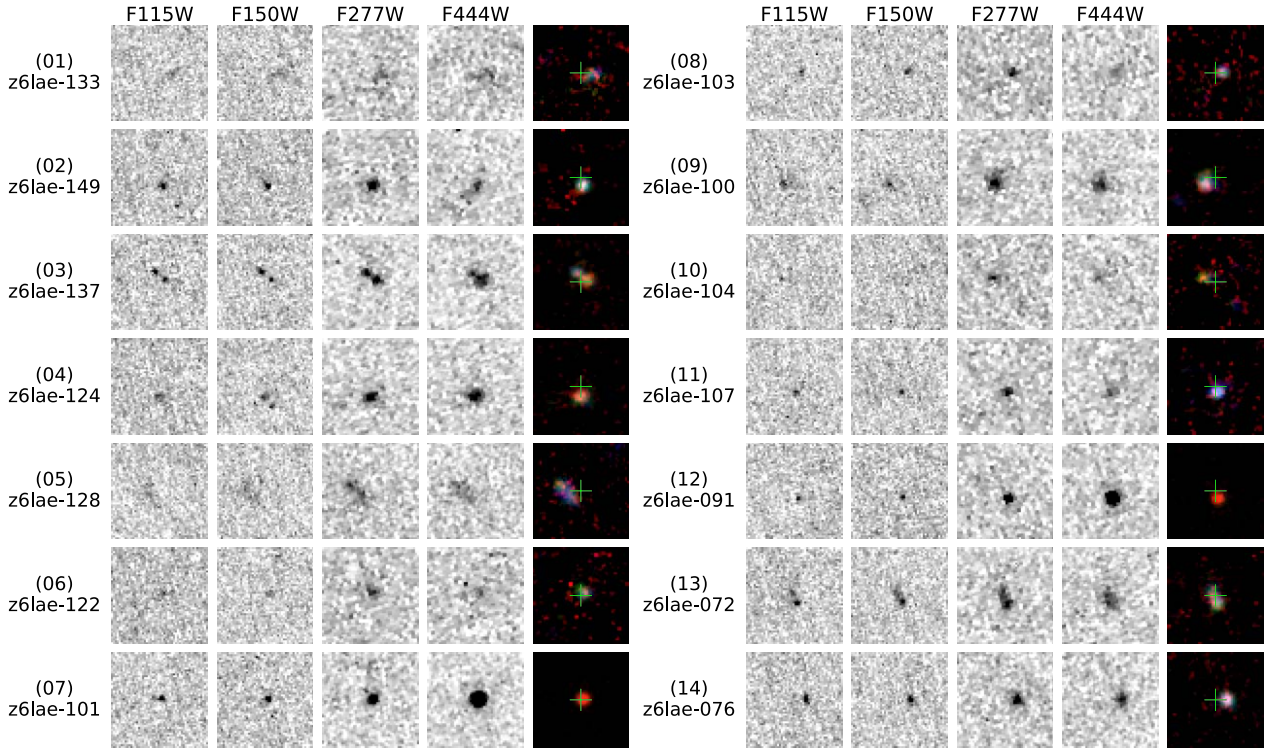

(c)

Figure 1. (a) Our LAE sample covered by the COSMOS-Web observations. The stars represent the 14 LAEs, in which the larger ones with thick edges indicate the merging/interacting systems (Section 4.1), while the red filled ones indicate the little red dots with AGN features (Section 4.2). The magenta pentagons correspond to all other $z \approx 5.7$ LAEs spectroscopically confirmed by our M2FS spectroscopic survey. The visit tiles covering our sample have a darker edge with the observation IDs (Column (5) in Table 1). The big circles represent the M2FS pointings. (b) The lower panel gives the redshift–Lyα luminosity distribution of the LAEs. The symbols are the same as those in panel (a). Note that two LAEs, z6lae-072 and z6lae-076, overlap each other in the parameter space. The corresponding number distributions are plotted shown in the upper panel. (c) The 14 LAEs detected in the four JWST/NIRCam bands ($1\farcs5 \times 1\farcs5$; north is up and east to left) with pseudo-color images (after PSF matching; blue: F115W+F150W; green: F277W; red: F444W). The central plus signs mark the Lyα centroids detected from the NB816 images.

Table 1
Observational Information of the $z \approx 5.7$ LAEs (Currently) Covered by COSMOS-Web

ID	R.A. (J2000.0)	Decl. (J2000.0)	$z_{\mathrm{Ly}\alpha}$	ObsID	NB816 (mag)	F115W (mag)	F150W (mag)	F277W (mag)	F444W (mag)
(1)	(2)	(3)	(4)	(5)	(6)	(7)	(8)	(9)	(10)
z6lae-133	09:59:08.43	+02:08:47.3	5.688	o080-t014	25.86 ± 0.11	27.67 ± 0.27	27.74 ± 0.23	27.72 ± 0.12	27.45 ± 0.09
z6lae-149	09:59:54.52	+02:15:16.6	5.689	o087-t045	24.66 ± 0.03	26.51 ± 0.13	26.89 ± 0.15	26.60 ± 0.05	26.62 ± 0.06
z6lae-137	09:59:54.78	+02:10:39.3	5.665	o089-t053	24.31 ± 0.02	26.56 ± 0.08	26.68 ± 0.07	26.41 ± 0.04	26.13 ± 0.04
z6lae-137a	09:59:54.77	+02:10:39.3	5.665	o089-t053	⋯	27.44 ± 0.13	27.83 ± 0.15	27.04 ± 0.05	26.60 ± 0.04
z6lae-137b	09:59:54.78	+02:10:39.4	5.665	o089-t053	⋯	27.20 ± 0.10	27.14 ± 0.08	27.30 ± 0.06	27.26 ± 0.07
z6lae-124	10:00:01.61	+02:06:20.4	5.705	o092-t062	25.31 ± 0.06	27.20 ± 0.25	26.91 ± 0.16	26.55 ± 0.05	25.99 ± 0.04
z6lae-128	10:00:05.04	+02:07:17.1	5.706	o092-t062	24.96 ± 0.04	27.02 ± 0.15	26.94 ± 0.11	27.03 ± 0.06	26.95 ± 0.07
z6lae-128a	10:00:05.05	+02:07:17.0	5.706	o092-t062	⋯	27.35 ± 0.15	27.87 ± 0.18	27.87 ± 0.09	27.65 ± 0.09
z6lae-128b	10:00:05.06	+02:07:17.1	5.706	o092-t062	⋯	>28.79	27.54 ± 0.13	27.71 ± 0.08	27.77 ± 0.10
z6lae-122	10:00:07.12	+02:05:57.0	5.666	o094-t070	25.70 ± 0.08	27.54 ± 0.32	27.87 ± 0.34	27.25 ± 0.08	27.48 ± 0.11
z6lae-101	10:00:19.97	+02:01:03.3	5.648	o098-t086	24.80 ± 0.04	26.75 ± 0.17	26.54 ± 0.11	26.00 ± 0.04	24.34 ± 0.01
z6lae-103	09:59:23.66	+02:02:14.4	5.724	o123-t039	25.53 ± 0.06	27.22 ± 0.23	27.64 ± 0.27	27.52 ± 0.11	27.14 ± 0.09
z6lae-100	09:59:44.06	+02:00:50.7	5.689	o127-t055	24.63 ± 0.03	26.20 ± 0.12	26.42 ± 0.12	26.32 ± 0.05	26.11 ± 0.04
z6lae-104	09:59:48.97	+02:02:27.1	5.652	o127-t055	25.97 ± 0.08	28.11 ± 0.49	>28.53	27.77 ± 0.11	27.70 ± 0.11
z6lae-107	09:59:50.75	+02:03:10.7	5.690	o127-t055	25.28 ± 0.05	26.50 ± 0.15	26.96 ± 0.19	27.14 ± 0.07	27.12 ± 0.08
z6lae-091	09:59:52.60	+01:57:01.1	5.728	o132-t072	25.32 ± 0.05	27.94 ± 0.46	27.61 ± 0.28	26.62 ± 0.05	25.01 ± 0.02
z6lae-072	10:01:02.95	+01:51:44.8	5.670	o147-t135	24.54 ± 0.03	26.36 ± 0.07	26.37 ± 0.06	26.26 ± 0.04	26.09 ± 0.05
z6lae-072a	10:01:02.95	+01:51:44.9	5.670	o147-t135	⋯	27.43 ± 0.13	27.31 ± 0.09	27.21 ± 0.07	26.92 ± 0.07
z6lae-072b	10:01:02.95	+01:51:44.7	5.670	o147-t135	⋯	26.87 ± 0.08	26.97 ± 0.07	26.84 ± 0.05	26.77 ± 0.06
z6lae-076	10:01:07.36	+01:52:22.7	5.670	o147-t135	24.59 ± 0.03	26.78 ± 0.13	26.79 ± 0.10	26.86 ± 0.06	26.71 ± 0.05

Note. The target coordinates are from the original LAE catalog given by NB detections (Ning et al. 2020), except for the components of the merging systems with suffixes *a* and *b* (the NB magnitudes are not shown), which are given by the NIRCam detections. The ">" symbols indicate 2σ upper limits.

GALFIT (see Section 3.1). We perform simulations to evaluate the flux uncertainty. For each galaxy (detected in the band), we create 100 mock sources (from GALFIT) and put them randomly (around the galaxy) on the given image. We then use SExtractor to do photometry as we did previously for the real objects, and we compute the mean and standard deviation of the measurements. Table 1 lists the multiband photometry results of the galaxy sample.

3. Results

In this section, we present the results of a variety of galaxy properties. We first study the galaxy morphology and then constrain the rest-frame UV continua. Next, we perform spectral energy distribution (SED) fitting to constrain their stellar mass (M_*) and star formation rates (SFR). We also utilize previous Lyα data to investigate the misalignment between the Lyα and UV emission. The results are summarized in Table 2.

3.1. Target Appearance and Morphology

As shown in Figure 1(c), most of the LAEs in our sample are either compact or irregular in the JWST/NIRCam images. Besides these, three LAEs (z6lae-072, z6lae-128, and z6lae-137) are resolved with interacting or double-component features. With Lyα redshifts, we obtain their projected distances of 0.″16 (0.93), 0.″23 (1.32), and 0.″19 (1.12 kpc), respectively. It is almost impossible that one of the components is a foreground or background object, due to a very low probability ($\lesssim$1%) that two random sources are located within an angular distance of 0.″2 (Fu et al. 2024). Among the three LAEs, only z6lae-137 is covered by HST/ACS F606W imaging observations. No detection (3σ upper limit of 27.8 mag in an aperture with a radius of 0.″15) exists at the positions of its two components, which supports that they are both at $z > 5$. Note that we cannot confirm robust (major or minor) mergers without the velocity-separation information from rest-frame optical spectra (e.g., Ventou et al. 2017; Dai et al. 2021). As the luminous LAEs are usually small with a typical size of $\lesssim$0.5 kpc (see our following result of galaxy sizes), the components do not tend to represent star-forming clumps within the same galaxy. They are thus probably in an advanced merging stage owing to their close proximity, and when considering merger events occur more frequently at high redshift (e.g., Rodriguez-Gomez et al. 2015). In this work, we also refer to them using the term "pair" for brevity.

In this work, we measure galaxy size to quantify the morphology of the LAEs (and their components). We use the half-light radius R_e, the radius containing half of the total light, to represent the galaxy size. We measure the galaxy size at the rest-frame UV band, which falls in the NIRCam SW bands with higher resolution than the LW bands. Before the measurement, we combine both F115W (with the PSF matched to F150W) and F150W bands to create stacking rest-UV images with higher S/N. As F115W and F150W bands are next to each other in the wavelength range, we ignore the effect of the morphological *k*-correction. The stacked images thus correspond to the rest-frame UV continuum without the influence from strong nebular emission lines for our galaxy sample. We run GALFIT (Peng et al. 2002, 2010) to directly measure the intrinsic effective radius by modeling a Sérsic profile. For each LAE covered by different visit tiles of COSMOS-Web, we adopt an empirical PSF by coadding at least 20 bright (not saturated) stars in each F150W tile image. The measured R_e (along the semimajor axis) is then circularized to represent the galaxy size by multiplying by the square root of the corresponding axis ratio. The GALFIT results are listed in Column (5) of Table 2. Note that no size is shown for z6lae-104 owing to its faintness in both F115W and F150W.

Table 2
Measured Properties of the LAE Sample at Redshift 5.7

ID	$\log_{10} L(\mathrm{Ly}\alpha)$ (erg s^{-1})	$\mathrm{EW}_0(\mathrm{Ly}\alpha)$ (Å)	$\Delta d_{\mathrm{Ly}\alpha}$ (kpc)	R_e (kpc)	M_{UV}	β_{UV}	$\log_{10} M_*$ ($M_\odot$)	SFR ($M_\odot$ yr^{-1})
(1)	(2)	(3)	(4)	(5)	(6)	(7)	(8)	(9)
z6lae-133	42.45 ± 0.17	125 ± 50	1.27 ± 0.60	0.47 ± 0.10	-18.98 ± 0.42	-2.26 ± 1.25	$8.56^{+0.15}_{-0.24}$	$1.34^{+0.69}_{-0.33}$
z6lae-149	42.90 ± 0.09	107 ± 21	0.62 ± 0.28	0.18 ± 0.03	-20.28 ± 0.21	-3.31 ± 0.70	$8.69^{+0.17}_{-0.22}$	$3.71^{+1.01}_{-0.68}$
z6lae-137	43.24 ± 0.05	272 ± 33	0.80 ± 0.23	...	-20.10 ± 0.13	...	...	...
z6lae-137a	...	...	...	<0.21	-19.36 ± 0.21	-3.38 ± 0.69	$9.12^{+0.07}_{-0.09}$	$3.06^{+1.01}_{-0.59}$
z6lae-137b	...	...	...	0.13 ± 0.04	-19.37 ± 0.16	-1.77 ± 0.47	$8.25^{+0.16}_{-0.21}$	$2.75^{+1.18}_{-0.65}$
z6lae-124	42.69 ± 0.15	166 ± 59	0.84 ± 0.41	0.28 ± 0.04	-19.28 ± 0.38	-1.00 ± 1.04	$9.27^{+0.13}_{-0.19}$	$8.72^{+2.90}_{-2.60}$
z6lae-128	42.83 ± 0.09	177 ± 39	1.11 ± 0.33	...	-19.55 ± 0.23	...	...	...
z6lae-128a	...	...	...	0.22 ± 0.12	-19.51 ± 0.24	-3.80 ± 0.82	$8.18^{+0.20}_{-0.20}$	$1.47^{+0.44}_{-0.32}$
z6lae-128b	...	...	...	0.65 ± 0.06	>-18.83	...	...	...
z6lae-122	42.61 ± 0.21	143 ± 67	0.60 ± 0.54	0.23 ± 0.08	-19.23 ± 0.51	-3.17 ± 1.63	$8.68^{+0.14}_{-0.30}$	$3.15^{+4.89}_{-1.80}$
z6lae-101	43.29 ± 0.11	428 ± 106	0.25 ± 0.30	0.10 ± 0.03	-19.74 ± 0.27	-1.27 ± 0.71	...	...
z6lae-103	42.62 ± 0.15	104 ± 36	0.54 ± 0.47	0.18 ± 0.05	-19.60 ± 0.37	-3.48 ± 1.25	$8.65^{+0.17}_{-0.23}$	$1.84^{+0.94}_{-0.51}$
z6lae-100	42.91 ± 0.08	86 ± 16	1.06 ± 0.27	0.51 ± 0.08	-20.52 ± 0.19	-2.79 ± 0.61	$8.99^{+0.11}_{-0.13}$	$4.91^{+1.32}_{-0.93}$
z6lae-104	42.70 ± 0.30	288 ± 197	1.31 ± 0.64	0.22 ± 0.14	-18.70 ± 0.74	...	...	...
z6lae-107	42.54 ± 0.10	44 ± 10	0.39 ± 0.40	0.22 ± 0.05	-20.35 ± 0.25	-3.64 ± 0.85	$8.25^{+0.18}_{-0.21}$	$3.05^{+0.80}_{-0.61}$
z6lae-091	42.77 ± 0.28	393 ± 251	0.61 ± 0.41	0.10 ± 0.05	-18.53 ± 0.69	-0.87 ± 1.89	...	...
z6lae-072	43.07 ± 0.05	161 ± 17	0.21 ± 0.26	...	-20.25 ± 0.11	...	...	...
z6lae-072a	...	...	...	0.13 ± 0.03	-19.11 ± 0.20	-1.57 ± 0.55	$8.74^{+0.12}_{-0.20}$	$2.31^{+1.23}_{-0.63}$
z6lae-072b	...	...	...	0.43 ± 0.05	-19.78 ± 0.13	-2.35 ± 0.38	$8.70^{+0.11}_{-0.18}$	$2.87^{+0.91}_{-0.46}$
z6lae-076	43.07 ± 0.08	239 ± 45	1.01 ± 0.27	0.22 ± 0.03	-19.83 ± 0.20	-2.03 ± 0.58	$8.65^{+0.13}_{-0.16}$	$3.17^{+0.84}_{-0.55}$

Note. The "<" sign indicates 2σ upper limits.

The intrinsic half-light radius R_e is plotted as a function of M_{UV} in the bottom panel of Figure 2. All of the LAEs lie below the average value of R_e shown by the gray shaded regions. Note that among the sample the two reddest LAEs in F277W–F444W (z6lae-091 and z6lae-101) have smallest sizes close to the PSF. For the rest, R_e are between 0.1 and 0.7 kpc with a median R_e of ≈0.2 kpc. Such statistics show broad consistency with Jiang et al. (2013a), which obtained a median R_e of ∼0.9 kpc, because our UV-fainter sample naturally appears smaller considering the size–luminosity relation. The individual galaxies in merging/interacting systems span a similar R_e range. Our results are also broadly consistent with other previous works about high-z LAEs based on HST imaging data (e.g., Taniguchi et al. 2009; Paulino-Afonso et al. 2018). The size–luminosity relation is not apparent for our sample, whose number of sources is currently limited.

3.2. Rest-frame UV Continua

Thanks to the deep near-IR photometry based on the JWST facilities, we can constrain weak UV continua of the faint galaxies. We measure the galaxy UV continua following our previous work (Ning et al. 2023). In this measurement, two objects, z6lae-104 and z6lae-128b, are discarded owing to the $<2\sigma$ detection(s) in F115W or F150W bands. Within the rest of the sample, only one source (z6lae-122) does not have $>4\sigma$ detections in both F115W and F150W. For all other sources with $>4\sigma$ detections in at least one SW band, the other band still has $>3\sigma$ detections except z6lae-091.

We assume a power-law form for the UV continuum of each source, i.e., $f_\lambda \propto \lambda^\beta$. In AB magnitude units, it has a linear relation $m_{\mathrm{AB}} \propto (\beta + 2) \times \log(\lambda)$. We then constrain the UV continuum using the SW photometric data for each source. We thus estimate the UV-continuum slope β with a single UV color. For our LAE sample at $z \approx 5.7$, F115W and F150W do not cover Lyα emission. We next subtract the UV continuum from the NB816 photometry to reconstrain Lyα flux (luminosity) and estimate the Lyα equivalent width EW_0(Lyα). The intergalactic medium (IGM) absorption blueward of Lyα line is considered in the computation based on the model from Madau (1995). The magnitude errors propagate into the measured UV quantities.

We plot the Lyα luminosity as a function of the absolute UV magnitude in Figure 2 (top panel). The measured M_{UV} of the sample range between -20.5 and -18.5 with a median value of -19.7. The Lyα luminosity has a potential dependence on M_{UV}. Note that none of the LAEs have $M_{\mathrm{UV}} < -20.6$ in our sample. The sample also shifts toward fainter UV luminosities when comparing to other samples. The reason is that Jiang et al. (2013b) exclude galaxies whose broadband photometry has weak detections of $<5\sigma$ in the J band or $<3\sigma$ in any other band.

In the middle panel of Figure 2, we show the relation between β and M_{UV}. Our sample has a broad β range roughly from -3.5 to -1.0. The median value is $\beta = -2.35 \pm 0.42$ which is broadly consistent with previous works (e.g., Finkelstein et al. 2012; Jiang et al. 2013b; Bouwens et al. 2014; Simmonds et al. 2023). But the luminous LAEs in our sample are overall bluer. Among them, six sources, including two components in the merging/interacting systems, have possibly extreme UV slopes of $\beta < -3$ with a mean of -3.46 ± 0.43. The extreme blue slopes usually indicate the existence of very young populations with low metallicity (e.g., Jiang et al. 2020; Topping et al. 2022). It is worth noting that for z6lae-137, which is a close pair, the two components have very different UV slopes. Their internal properties are thus supposed to be largely diverse, such as the dust attenuation, metallicity, and age of the stellar populations, which also supports that they are two individual galaxies in the merging

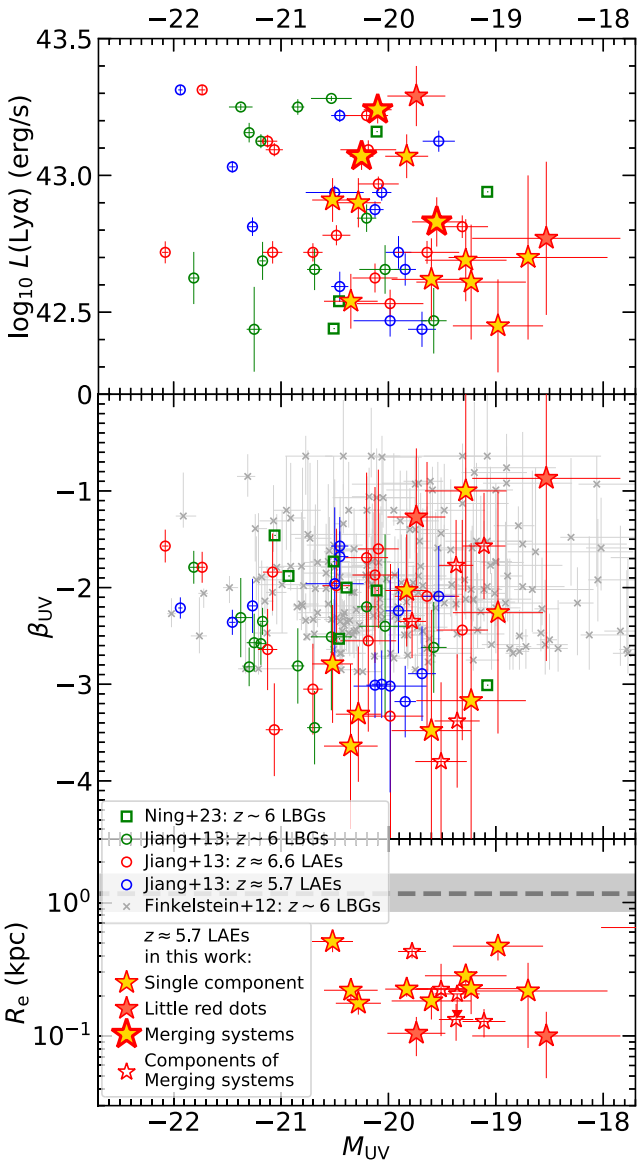

Figure 2. Lyα luminosity (top panel), UV slope (middle panel), and half-light radius (bottom panel) as a function of the absolute UV magnitude at rest-frame 1500 Å. The stars indicate the 14 LAEs at $z \approx 5.7$ in this work. Note that the larger stars with thick edges mark the merging/interacting systems and the smaller open ones mark their individual components. The green squares represent the LBGs (luminous in Lyα) at $z \simeq 6$ from Ning et al. (2023). The open circles correspond to the LBGs at $z \simeq 6$ (green) and LAEs at $z \approx 5.7$ (blue) and 6.5 (red) from Jiang et al. (2013b). The gray crosses represent the LBGs at $z \sim 6$ from Finkelstein et al. (2012). In the bottom panel, the gray dashed line with an uncertainty region indicates an average R_e for galaxies at $z \approx 5.7$, which is obtained from the size–evolution results of Ormerod et al. (2024).

system (in comparison with the sample from Bolamperti et al. 2023). The above results need to be verified by larger samples with more accurate UV-slope measurements from more JWST SW bands.

3.3. Physical Properties

We constrain the physical properties of the 14 LAEs at $z \approx 5.7$ by adopting SED fitting. These LAEs have spectroscopic redshifts from Lyα lines. The spectroscopic redshift is a significant parameter when performing SED fitting. Without the secure redshift, the nebular lines of galaxies may be set into wrong filter bands. We adopt the SED fitting tool `Bagpipes` (Carnall et al. 2018). `Bagpipes` provides a Python framework for self-consistently modeling the stellar, nebular, dust, and IGM properties of galaxy spectra.

A small fraction of our sample is very blue, with likely extreme slopes of $\lesssim -3$. Jiang et al. (2020) studied six very blue LAEs at $z \simeq 6$. They found that young populations without dust content can produce very blue slopes reaching $\beta \simeq -3$, but the SED models cannot produce extreme slopes of $\beta < -3$. This work used three or four photometric data points to obtain relatively reliable UV slopes. However, we currently compute the UV slopes based on the two SW bands. As the UV slopes are not robust enough, with large errors due to only two (low-S/N) SW photometric data, we keep adopting a standard SED fitting procedure based on `Bagpipes` even for the bluest LAEs in this work. The results show that the best-fit SED models agree with the observational photometry within the uncertainty range, although they cannot perfectly match the UV colors. Two galaxies (z6lae-128b and z6lae-104) in our sample are not detected ($<3\sigma$) in F115W or F150W. We thus do not perform SED fitting to them, as they have photometric data in only three bands, although we can estimate limitations for their UV luminosities.

We choose to use the double power-law model to parameterize the star-forming history of our galaxies. We perform the SED fitting within a broad parameter space. The falling slope and the rising slope are assigned to vary in the logarithmic ranges of -8 to 2 and -2 to 8, respectively. The timescale τ (related to the SFR peak time) varies across the whole cosmic time. We assume a Calzetti law (Calzetti et al. 2000) for dust attenuation, with absolute attenuation in the V band (A_V) varying between 0 and 4 mag. The metallicity is set within the range of 0.001–10 times the solar metallicity. The formed mass varies in the logarithmic range of 7–13. We also include the CLOUDY model nebular emission with ionization parameter of $-4 < \log(U) < -1$. The observed and best-fit model SEDs are shown in Figure 3. We get proper fitting results for most of our sources except z6lae-091 and z6lae-101 (see panels 06 and 11 in Figure 3), which both have very red F277W–F444W colors. We discuss the two sources in the next section.

We obtain SFR and M_* for each LAE in our sample. The SFR–M_* distribution of our sample is plotted in the left panel of Figure 4. We also compare our results with the best-fit main-sequence (MS) relations of star-forming galaxies at $z \sim 3$–6.5 from Rinaldi et al. (2022). Note that the evolution of the slopes is negligible in the redshift range. We can see that our LAEs lie around the MS relation and the five individual galaxies in the merging/interacting systems overall coincide with the LAEs with single components. Part of them exhibit a potentially weak-burst mode. Despite the large scatter, they populate broadly in accord with the bimodal distribution indicated by the young and old LAEs (e.g., Iani et al. 2023).

We also investigate the relation between the galaxy size and stellar mass of our sample. The galaxy size is the effective radius R_e, which is measured from the stacked SW (F115W and F150W) images. Our results are plotted in the right panel of Figure 4. We compare with the results of Langeroodi & Hjorth (2023). Our results overall populate below their best-fit linear function of the mass–size relation over a redshift range of $z \sim 4$–10. Note that its intercept has a significant scatter of

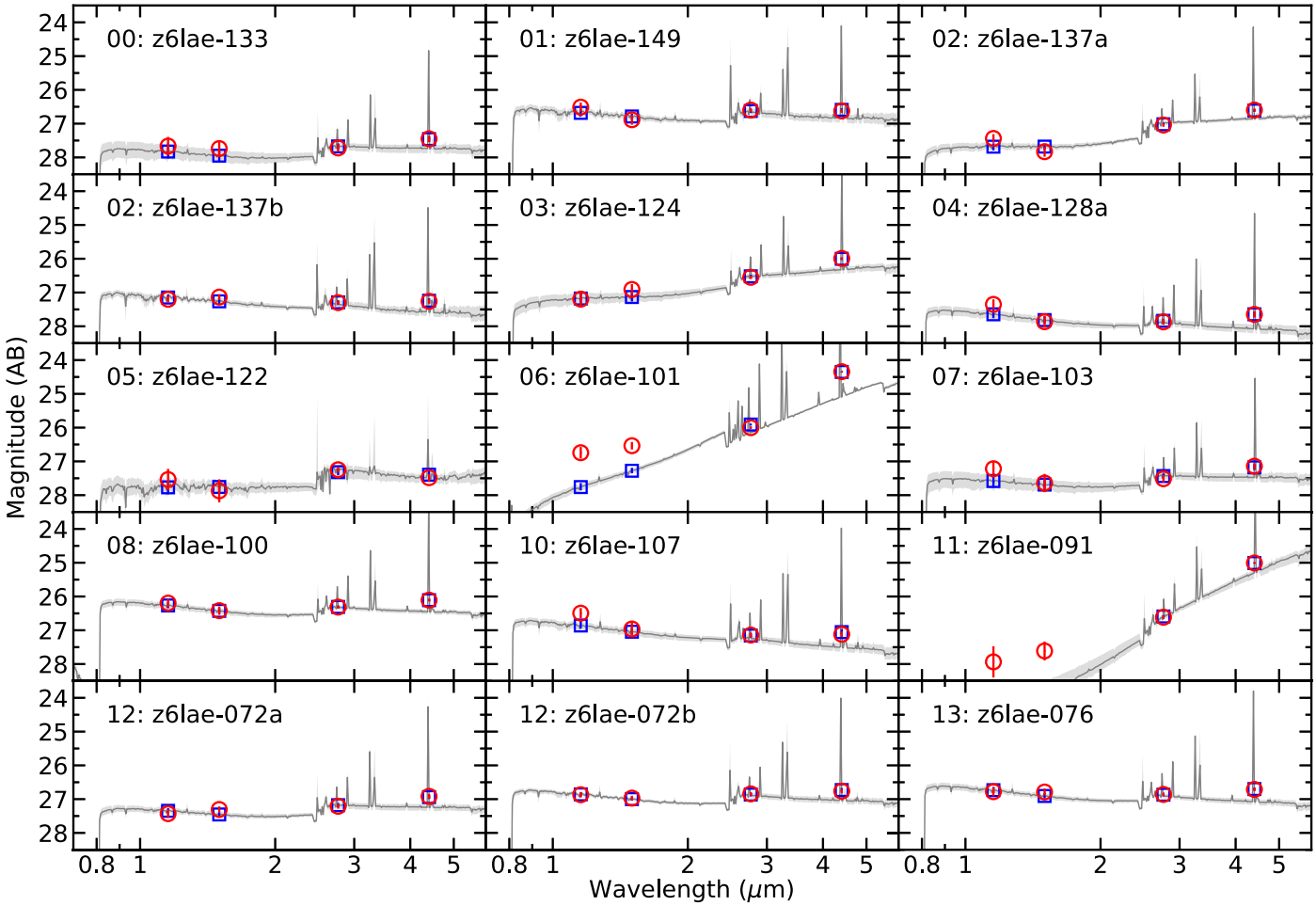

Figure 3. SED fitting for our LAE sample with `Bagpipes`. In each panel, the observed and best-fit photometric data are shown by red circles and blue squares with error bars, respectively. The best-fit model SED is plotted as a gray line with a shaded region indicating 1σ uncertainty. Note that the best-fit model SEDs cannot match the observed SEDs for the two little red dots, z6lae-091 and z6lae-101, which imply probably additional AGN components.

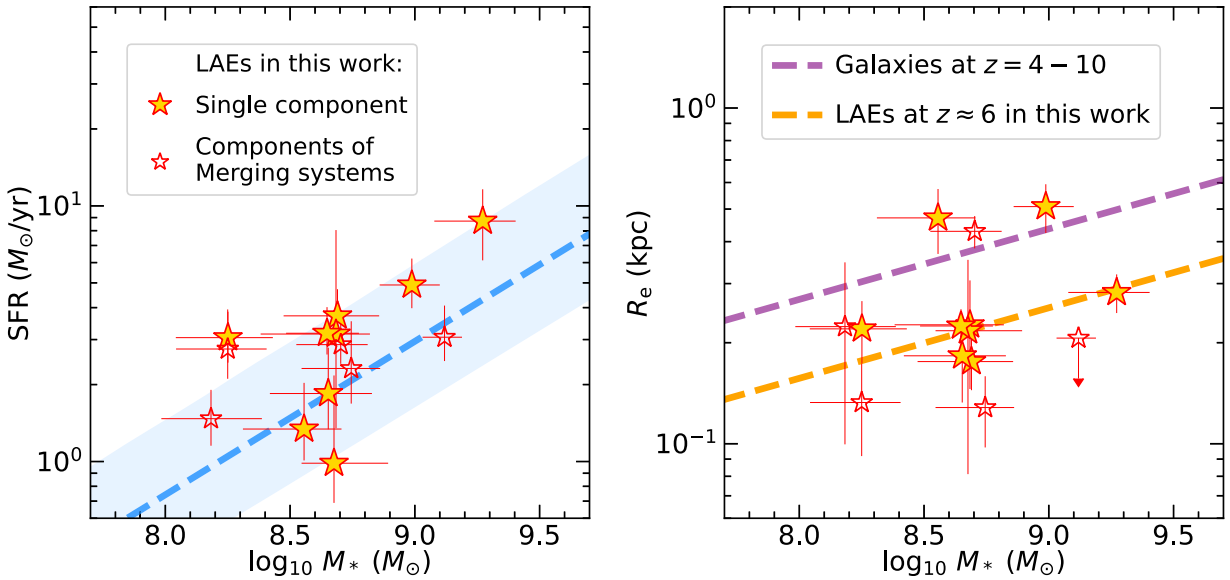

Figure 4. The SFR–M_* and size–M_* distributions of our LAE sample. The stars indicate our sample of 14 LAEs at $z \approx 5.7$; the smaller open ones mark the components of the merging/interacting systems. In the left panel, the blue lines represent the best-fit MS power-law relation from Rinaldi et al. (2022). In the right panel, the orange dashed line is the best-fit linear relation for our LAEs at $z \approx 5.7$. The purple line gives the mass–size relation for galaxies at $z = 4$–10 from Langeroodi & Hjorth (2023).

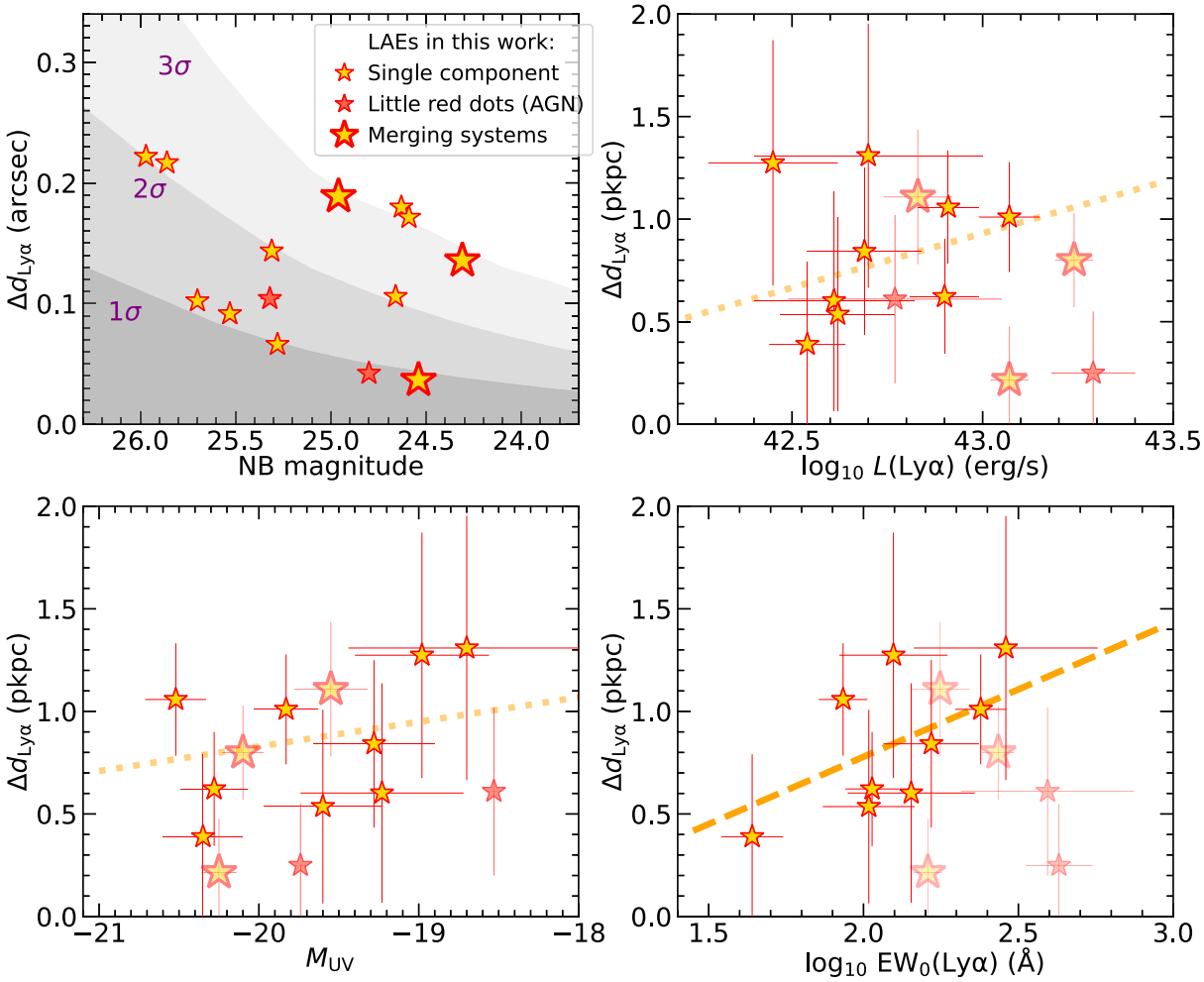

Figure 5. Lyα–UV spatial offset $\Delta d_{\mathrm{Ly}\alpha}$ as a function of NB magnitude, Lyα luminosity, rest-frame UV magnitude, and Lyα equivalent width. The stars indicate the 14 LAEs at $z \approx 5.7$ in this work, while the larger ones with thick red edges mark the merging/interacting systems and the red filled ones mark the two LAEs (z6lae-091 and z6lae-101) probably hosting AGNs. In the top left panel, the $\Delta d_{\mathrm{Ly}\alpha}$ are plotted in units of arcsec with the shaded regions of measurement uncertainty for the NB imaging detection. In the other panels, the $\Delta d_{\mathrm{Ly}\alpha}$ are plotted in units of physical kpc (pkpc) with 1σ error bars converted from the 1σ curve shown in the top left panel. The orange dotted and dashed lines indicate the best-fit linear functions. We also make the merger and AGN symbols shallower to highlight, by contrast, the LAEs used in the linear fitting.

$\sim$0.3 dex. The sample potentially displays an overall upward trend. As our sample size limits the accurate fitting analysis, we perform linear regression fitting with the same fixed slope as that of Langeroodi & Hjorth (2023). We obtain a best-fit linear relation lower than that of Langeroodi & Hjorth (2023) by $>$0.2 dex. The (rest-frame) UV compactness of the LAEs implies that they tend to be metal-deficient (e.g., Langeroodi & Hjorth 2023) and thus dust-poor, which agrees with our (SED-fitting-derived) dust extinction of $E(B-V) < 0.1$ for our LAEs. Such an interstellar medium (ISM) environment may facilitate their Lyα escape from star-forming regions even if there are bursty activities or rapid gas accretion.

3.4. Lyα–UV Misalignment

We investigate the misalignment between Lyα and UV emission for the LAEs in our sample. In this work, we compare the Lyα centroid in the Suprime NB images and (rest-frame) UV centroid in the JWST/NIRCam images. For the three merging/interacting systems in our sample (z6lae-072, z6lae-128, and z6lae-137), we adopt the positional center of all components as the original position. When evaluating the Lyα–UV projected offsets ($\Delta d_{\mathrm{Ly}\alpha}$), we consider both accuracy and precision on the astrometry. We first address the astrometric accuracy by eliminating the overall systematic WCS offsets between the COSMOS NB image and each JWST COSMOS-Web tile. In this procedure, all detected sources in each tile are compared to their counterparts in the NB image. We thus have the median value for each two-dimensional (2D) distribution of the positional differences. The COSMOS-Web tiles have WCS systematic offsets relative to the NB image in the range of $\sim$0.″01–0.″04.

For the abovementioned (2D) distributions, the dispersion degree basically reflects the astrometric precision. But it depends on the brightness and morphology of sources. In this work, we address the astrometric precision by estimating the measurement uncertainty, which mainly comes from detection measurements in the NB image. The reason is as follows. For galaxies at $z \sim 6$, a typical size of 1 kpc corresponds to $\lesssim$0.″2. The COSMOS NB816 image has a PSF FWHM of $\sim$0.″5, overwhelmingly larger than those of the NIRCam SW bands. The measurement uncertainty thus influences the positional information of source detection, especially for the faint targets. Such errors could be even comparable with their intrinsic sizes. We thus need to evaluate how the detected Lyα centroid

deviates from its original position. We implement a Monte Carlo simulation to measure the distribution of the positional offsets as a function of NB brightness. The simulation is similar to that conducted in our previous work (see Section 4.1.1 in Ning et al. 2022). Below we simply describe the main procedures.

We first obtain a PSF of the COSMOS NB816 image and create a mock LAE by convolving the PSF difference kernel with the stacked LAE image based on a large sample of LAEs at $z \approx 5.7$ (Ning et al. 2020). We then simulate a large number of mock LAEs with a series of magnitudes and insert them randomly into the COSMOS NB816 image. In the meantime, we record the original positions of the mock LAEs falling on the image. Next, we run `SExtractor` to detect the corresponding mock sources. For the detected ones, we compute their positional differences from their original positions. We obtain a series of 2D normal distributions of the positional offsets whose standard derivations are an increasing function as the source brightness gets fainter. The standard derivation represents the measurement error when evaluating the positional difference for the mock sources falling in the image. We finally interpolate and produce the measurement errors using the detected NB magnitude for each LAE. The results are consistent with the 2D positional difference distributions mentioned in the first paragraph of this section.

In Figure 5, we show the $\Delta d_{\mathrm{Ly}\alpha}$ as a function of NB magnitude, Lyα luminosity, rest-frame UV magnitude, and Lyα equivalent width. We overplot the gray shaded regions of the measurement errors from source detection in NB imaging in the top left panel. The results of our measured $\Delta d_{\mathrm{Ly}\alpha}$ are listed in units of kpc in Column (4) of Table 2. For the luminous LAEs in our sample, the misalignment of Lyα and UV emission has offsets in the range of $\Delta d_{\mathrm{Ly}\alpha} \sim$0–1.5 kpc with a median value of $\sim$0.7 kpc. Half of our sample has large $\Delta d_{\mathrm{Ly}\alpha}$ at a significant level of $\gtrsim 2\sigma$. The $\Delta d_{\mathrm{Ly}\alpha}$ are more than twice as large as the half-light radii of the LAEs on average. Previous studies also report a significant Lyα–UV offset for most of the Lyα-emitting galaxies (e.g., Hoag et al. 2019; Lemaux et al. 2021; Claeyssens et al. 2022). Note that the $\Delta d_{\mathrm{Ly}\alpha}$ range of our LAE sample does not exceed a typical Lyα–halo scale length of $\sim$2 kpc (Wu et al. 2020).

Our results reveal the nonnegligible misalignment between the Lyα and UV centroids for the LAEs, especially those with high EW_0(Lyα). The Lyα–UV misalignment corresponds to a positional offset reaching more than $0\farcs2$ for galaxies at $z \lesssim 6$. If the redshift goes higher, for those targets of interest for JWST spectroscopic observations (while the Lyα line can fall into the JWST wavelength coverage), such angular offset becomes larger. However, for JWST/NIRSpec (multiobject) spectroscopy, the slit width (in the dispersion direction) of each MSA shutter is just $0\farcs2$. Thus, a significant proportion of Lyα emission would be probably lost besides the slit losses if the shutter is aligned mainly to the UV counterparts. Such systematic offset of Lyα emission should not be ignored when it is observed by JWST slit spectroscopy for galaxies in the epoch of reionization.

4. Discussion

In this section, we discuss the merger/interacting systems and probable active galactic nuclei (AGNs) in our LAE sample. We also discuss the possible relation between $\Delta d_{\mathrm{Ly}\alpha}$ and EW_0(Lyα).

4.1. Potential Mergers in the LAE Sample

In the sample, three LAEs (z6lae-072, z6lae-128, and z6lae-137) displaying galaxy pairs are potential merging/interacting systems as shown in Figure 1(c). The number ratio (3/14) of the whole sample is similar to that of a recent study on LAEs at $z \approx 3.1$ (2/10; Liu et al. 2023). Among the three merging systems, two are at the bright end of $-42.9 < \log_{10} L(\mathrm{Ly}\alpha) \leqslant -43.4$ or $-20.5 < M_{1500} \leqslant -19.5$, making a fraction of $\sim$30%, while one is at the faint end of $-42.4 < \log_{10} L(\mathrm{Ly}\alpha) \leqslant -42.9$ or $M_{1500} > -19.5$, giving a fraction of $\lesssim$20%. The extrapolation of the two percentages is well consistent with the value of 40%–50% at a brighter range of $M_{1500} \leqslant -20.5$ (Jiang et al. 2013a). It is worth noting that two LAEs at $z \approx 6.6$, Himiko and CR7, which are extremely luminous in Lyα, are both triple-component systems (Ouchi et al. 2013; Sobral et al. 2019). The result reveals a trend that the multicomponent fraction becomes larger as the systems get brighter in terms of Lyα or UV, which preferentially trace more overdense regions (e.g., Helton et al. 2023).

It is interesting to see that the three LAEs are very luminous in Lyα, especially two of them that are the brightest ones in our sample. But where the Lyα emission mainly originates from in the galaxy pairs is poorly resolved owing to the relatively low resolution of NB imaging observations. It is most likely contributed by the star-forming regions because components in merger systems intuitively have higher SFRs due to triggered bursty activity. However, for the three pairs, most of their components do not deviate from the star-forming MS relation as shown in the left panel of Figure 4. This illustrates that SFR is not apparently enhanced at the pair separation scale, which is consistent with previous results at lower redshift (e.g., Pearson et al. 2019; Dai et al. 2021). For z6lae-137, although one of the components, z6lae-137b, has a weak SB mode ($\sim$0.3 dex higher than the MS relation), the Lyα centroid is not located more closely to it in a close visual inspection. Hence, the merging/interacting systems probably favor that Lyα origin may occur in the circumgalactic medium (CGM) regions. In merger activities, strong interactions between the CGM of each component can induce gas cooling (e.g., Sparre et al. 2022; Gupta et al. 2023) and then produce additional Lyα emission.

4.2. Little Red Dots and AGNs

In the above SED fitting, we analyze our LAE sample assuming that they are all pure galaxies. However, the best-fit model SEDs cannot match the observed ones for two sources with the smallest galaxy sizes, z6lae-091 and z6lae-101, if we assume that they are pure galaxies. We thus consider the possible existence of AGN activity, which cannot be ruled out for high-z objects (e.g., Juodžbalis et al. 2023; Li et al. 2023; Lyu et al. 2023). Although the typical narrow Lyα lines in our LAE sample exclude the possibility of bright type 1 AGNs, the broad-line component of faint AGNs may also be drowned in the noise of (ground-based) Magellan/M2FS spectra, unlike the much more sensitive JWST/NIRSpec. Note that they also have the two highest EW_0(Lyα) in our sample, albeit with relatively large errors.

As seen in the images, z6lae-091 and z6lae-101 are both red compact sources featured as "little red dots" (e.g., Matthee et al. 2023; Williams et al. 2023). First, their PSF-like

morphology implies a nonnegligible AGN component (e.g., Barro et al. 2023). The two LAEs are also very red in terms of the F277W–F444W color. They have F277W–F444W $\gtrsim 1.6$, revealing a probability of hosting AGNs of at least 80% (Greene et al. 2023). The AGN fraction of our LAE sample is then $\frac{2}{14} \times 80\% \approx 0.11$, which is consistent with faint AGNs occupying $\sim$10% of the galaxy population at $z \sim 6$ (e.g., Harikane et al. 2023; Maiolino et al. 2023).

Although a strong Hα line may also boost the F444W band for $z \sim 6$ galaxies, it is worth noting that a bluer F277W–F444W color of <1.5 is shown by an LBG (from Ning et al. 2023) with an extremely high ionizing production efficiency of $\log_{10} \xi_{\rm ion,\,0}$ (Hz erg^{-1}) ≈ 26.5, which is a rare case in high-z galaxies (e.g., Rinaldi et al. 2023; Seeyave et al. 2023). In addition, the ALMA ALPINE survey has covered z6lae-101 in band 7 (Béthermin et al. 2020). The nondetections in both [C II] 158 μm line and far-IR continuum (3σ upper limits of 0.190 Jy km s^{-1} and 0.194 mJy, respectively) also disfavor that the dusty star formation results in such red optical continuum. Hence, pure galaxies (at $z \sim 6$) should hardly produce the very red F277W–F444W color. The AGN presence in the LAE population waits to be revealed with rest-frame optical spectra or images in other bands (such as MIRI) based on a larger sample.

4.3. Δd$_{Ly\alpha}$–EW_0(Lyα) Relation

Lyα emission provides useful information for probing the reionization process and physics of galaxies in this epoch. However, Lyα photons propagate with resonant scattering through complicated routines and suffer absorption in the ISM, the CGM, and the surrounding IGM (e.g., Hayes et al. 2011; Dijkstra 2014; Cai et al. 2017, 2019; Zhang et al. 2024). It is thus not surprising that Lyα emission is exhibited at different positions from the star-forming regions of galaxies. Meanwhile, many studies utilize such Lyα–UV (projected) offsets in turn to explore the Lyα escaping process. For example, Shibuya et al. (2014) show that some LAEs (at $z \sim 2.2$) have a spatial offset reaching $\sim$2.5–4 kpc between the Lyα and UV-continuum emission.

In Figure 5, the larger stars mark the merging/interacting systems, while the red filled ones indicate the two LAEs, z6lae-091 and z6lae-101, probably hosting AGNs. For the merging/interacting systems, the Lyα centroid is supposed to be modified by all components, which is a complex process. For the (type 2) AGNs, Lyα emission is radiated from not only the star-forming regions, but also the narrow-line regions (Osterbrock & Ferland 2006). If we ignore the LAEs hosting AGNs or the components in the bottom right panel, we can see that there is a likely positive correlation between $\Delta d_{\rm Ly\alpha}$ and EW$_0$(Lyα) with a fitting linear slope of 0.66 ± 0.37. The correlations become weaker in the $\Delta d_{\rm Ly\alpha}$–$M_{\rm UV}$ and $\Delta d_{\rm Ly\alpha}$–L(Lyα) parameter spaces. The Spearman correlation coefficients are 0.34 ± 0.24, 0.18 ± 0.26, and 0.12 ± 0.32 for the $\Delta d_{\rm Ly\alpha}$–EW$_0$(Lyα), $\Delta d_{\rm Ly\alpha}$–$M_{\rm UV}$, and $\Delta d_{\rm Ly\alpha}$–L(Lyα) relations, respectively, by perturbing the measured quantities with their uncertainties (e.g., Curran 2014). Note that the original coefficient 0.57 for $\Delta d_{\rm Ly\alpha}$–EW$_0$(Lyα) is largely reduced after perturbing the data set due to the small sample size and large uncertainty.

The $\Delta d_{\rm Ly\alpha}$–$M_{\rm UV}$ trend does not agree with Lemaux et al. (2021). They found that UV-brighter galaxies exhibit offsets $\sim$3 times larger than their UV-fainter counterparts. The reason for such inconsistency is unclear, but we notice that they measure the Lyα location based on the 2D spectra of Lyα lines through the slits. One of the possibilities might be that our LAEs are stronger in terms of EW$_0$(Lyα) while most of their sample has EW$_0$(Lyα) <100 Å. If we extrapolate our $\Delta d_{\rm Ly\alpha}$–$M_{\rm UV}$ trend into a range of $M_{\rm UV} \lesssim -22$ mag, the $\Delta d_{\rm Ly\alpha}$ of LAEs is supposed to be smaller, which is also consistent with Jiang et al. (2013a). They find that the observed Lyα location does not deviate from its original position in compact galaxies based on a UV-brighter sample.

Here we invoke a simple physical scenario to explain the marginal $\Delta d_{\rm Ly\alpha}$–EW$_0$(Lyα) relation. A basic picture is wrapped up inside the diffusion process of Lyα transfer in ISM (and/or CGM; Dijkstra 2014; Gronke et al. 2016). H I density or its covering fraction plays an important role to modify both $\Delta d_{\rm Ly\alpha}$ and EW$_0$(Lyα). If the H I gas is denser (or with higher covering fraction), Lyα emission will escape more difficultly from the original region (smaller $\Delta d_{\rm Ly\alpha}$), while the metallicity (and thus dust content; e.g., Popping et al. 2017) is correspondingly higher (Santini et al. 2014; Tacconi et al. 2020), inducing lower EW$_0$(Lyα) (and also lower Lyα escape fraction $f_{\rm esc}^{\rm Ly\alpha}$; e.g., Roy et al. 2023). Conversely, higher EW$_0$(Lyα) emission can wander off (anisotropically) more easily with larger $\Delta d_{\rm Ly\alpha}$ (Dayal & Ferrara 2018) in the less chemically enriched ISM (e.g., Maseda et al. 2023; Saxena et al. 2023). This scenario can also explain the previously found anticorrelation between Lyα velocity offset $\Delta v_{\rm Ly\alpha}$ and EW$_0$(Lyα) (Tang et al. 2021; Prieto-Lyon et al. 2023). As Lyα photons are scattered by H I, the offsets in real ($\Delta d_{\rm Ly\alpha}$) and frequency ($\Delta v_{\rm Ly\alpha}$) space couple with each other. The ionized bubble size can thus be estimated by large $\Delta d_{\rm Ly\alpha}$ misalignment, which is associated with low $\Delta v_{\rm Ly\alpha}$ (e.g., Mason & Gronke 2020) for the galaxies in the epoch of reionization. The above scenario can also be tested with additional $f_{\rm esc}^{\rm Ly\alpha}$ results based on more spectroscopic information including Balmer lines such as Hα.

5. Summary

In this work, we study a sample of LAEs at $z \approx 5.7$ based on JWST/NIRCam imaging data. The sample consists of 14 LAEs that have been spectroscopically confirmed with strong Lyα lines previously by our Magellan/M2FS survey. They spread a Lyα luminosity range of L(Lyα) $\sim 10^{42.4}$–$10^{43.4}$ erg s^{-1}. The JWST/NIRCam imaging data set comes from the COSMOS-Web program, which is still ongoing currently but has covered around half of the total designed survey area in the four NIRCam bands (F115W, F150W, F277W, and F444W). Our LAEs constitute a sample of luminous galaxies in terms of Lyα luminosity over a large survey area in this redshift slice.

We utilize the highly resolved, deep near- and mid-IR images to explore a variety of galaxy properties, including the rest-frame UV properties (luminosity, continuum slope, and size), stellar mass (M_*), and SFRs. We also investigate the misalignment of Lyα and UV emission for the LAEs at $z \approx 5.7$. We summarize our conclusions as follows:

1. The LAE sample is UV-faint between $M_{\rm UV} \sim -20.5$ and -18.5 mag. The UV-continuum slopes have a median value of $\beta \approx -2.35$ with a range from -3.5 to -1.0. These luminous LAEs in the sample are overall bluer. A fraction (6/15) of them (including the components)

exhibit very blue UV slopes of $\beta < -3$ with a mean of -3.46 ± 0.43.

2. With the galaxy SED modeling, we derive stellar mass and SFRs for the whole sample. Most of the LAEs or their components lie on the MS relation, while a small fraction of them show a weak-burst mode.
3. Our LAEs are overall compact in morphology. Besides the two point-like sources, the galaxy sizes R_e are between 0.1 and 0.7 kpc with a median R_e of $\approx$0.2 kpc. The LAEs are found substantially (>0.2 dex) below the overall mass–size relation of high-z galaxies.
4. Three of the 14 LAEs are distinguished as potential merging/interacting systems. Estimating the merger fraction at the bright and faint bins indicates that luminous LAEs (in UV or Lyα), which preferentially reside in more overdense regions, tend to be interacting systems. The gas cooling induced by the interaction may enhance Lyα luminosity.
5. Two LAEs in our sample probably own nonnegligible AGN components. Both of them are featured as "little red dots" with PSF-like morphology and very red color in F277W–F444W. The probability of our sample containing AGNs is roughly 10%, which is consistent with the AGN fractions obtained by previous works.
6. For our luminous sample of LAEs at redshift 5.7, the misalignment between Lyα and UV emission mostly exists with positional offsets $\Delta d_{\mathrm{Ly}\alpha}$ in the range of $\sim$0–1.5 kpc (a median value of $\sim$0.7 kpc). A positive correlation may exist between $\Delta d_{\mathrm{Ly}\alpha}$ and $\mathrm{EW}_0(\mathrm{Ly}\alpha)$, which could be established by varying H I density (and/or covering fraction) of the ISM and CGM. Such Lyα −UV offsets should be considered when conducting JWST slit spectroscopic observations if covering Lyα.

Our results reveal a diversity of the sources associated with LAEs, including AGNs, merging/interacting systems, and single star-forming galaxies. This work also highlights the powerful performance of JWST to study luminous LAEs at redshift $z \gtrsim 6$ over a relatively large sky area ($\sim$0.28 deg^2). We will extend our research by enlarging the sample and including the $z \approx 6.6$ LAEs confirmed by our spectroscopic survey with the entire data set from the COSMOS-Web survey. We also look forward to unraveling the nature of LAEs in the epoch of reionization with more JWST spectroscopic follow-up and imaging observations in the other bands.

Acknowledgments

We thank the COSMOS-Web group lead by J. S. Kartaltepe and C. M. Casey for contributing the JWST imaging dataset. We thank L. Jiang and J. Li for the instructive discussions. We thank Z. Sun for maintaining the high-performance computing platform of the high-redshift research group in the Department of Astronomy, Tsinghua University. We also thank the anonymous referee for the constructive comments and suggestions that improved this paper.

We acknowledge support from the National Key R&D Program of China (grant No. 2018YFA0404503), the National Science Foundation of China (grant No. 12073014), the science research grants from the China Manned Space Project with No. CMS-CSST-2021-A05, and the Tsinghua University Initiative Scientific Research Program (No. 20223080023). We also acknowledge the support from the Shuimu Tsinghua Scholar Program of Tsinghua University. Q. Li acknowledges support from the ERC Advanced Investigator Grant EPOCHS (788113).

This work is based on the observations made with NASA/ESA/CSA James Webb Space Telescope. JWST data are obtained from the Mikulski Archive for Space Telescopes (MAST) at the Space Telescope Science Institute, which is operated by the Association of Universities for Research in Astronomy, Inc., under NASA contract NAS 5-03127 for JWST. The JWST observations are associated with the program GO-1727.

Facility: JWST (NIRCam).

ORCID iDs

Yuanhang Ning https://orcid.org/0000-0001-9442-1217
Zheng Cai https://orcid.org/0000-0001-8467-6478
Xiaojing Lin https://orcid.org/0000-0001-6052-4234
Zhen-Ya Zheng https://orcid.org/0000-0002-9634-2923
Xiaotong Feng https://orcid.org/0000-0003-0174-5920
Mingyu Li https://orcid.org/0000-0001-6251-649X
Qiong Li https://orcid.org/0000-0002-3119-9003
Daniele Spinoso https://orcid.org/0000-0002-9074-4833
Yunjing Wu https://orcid.org/0000-0003-0111-8249
Haibin Zhang https://orcid.org/0000-0003-2273-9415

References

Adams, N. J., Conselice, C. J., Ferreira, L., et al. 2023, MNRAS, 518, 4755
Ashby, M. L. N., Willner, S. P., Fazio, G. G., et al. 2015, ApJS, 218, 33
Barro, G., Perez-Gonzalez, P. G., Kocevski, D. D., et al. 2023, arXiv:2305.14418
Bertin, E., & Arnouts, S. 1996, A&AS, 117, 393
Béthermin, M., Fudamoto, Y., Ginolfi, M., et al. 2020, A&A, 643, A2
Bolamperti, A., Zanella, A., Meštrić, U., et al. 2023, MNRAS, 526, 5263
Bouwens, R. J., Illingworth, G. D., Oesch, P. A., et al. 2014, ApJ, 793, 115
Bradač, M. 2020, NatAs, 4, 478
Bradley, L. D., Coe, D., Brammer, G., et al. 2023, ApJ, 955, 13
Bushouse, H., Eisenhamer, J., Dencheva, N., et al. 2022, JWST Calibration Pipeline, v.1.7.2, Zenodo, doi:10.5281/zenodo.7071140
Cai, Z., Cantalupo, S., Prochaska, J. X., et al. 2019, ApJS, 245, 23
Cai, Z., Fan, X., Yang, Y., et al. 2017, ApJ, 837, 71
Calzetti, D., Armus, L., Bohlin, R. C., et al. 2000, ApJ, 533, 682
Carnall, A. C., McLure, R. J., Dunlop, J. S., & Davé, R. 2018, MNRAS, 480, 4379
Casey, C. M., Kartaltepe, J. S., Drakos, N. E., et al. 2023, ApJ, 954, 31
Castellano, M., Fontana, A., Treu, T., et al. 2022, ApJL, 938, L15
Claeyssens, A., Richard, J., Blaizot, J., et al. 2022, A&A, 666, A78
Curran, P. A. 2014, arXiv:1411.3816
Curtis-Lake, E., McLure, R. J., Pearce, H. J., et al. 2012, MNRAS, 422, 1425
Dai, Y. S., Malkan, M. M., Teplitz, H. I., et al. 2021, ApJ, 923, 156
Dayal, P., & Ferrara, A. 2018, PhR, 780, 1
Dijkstra, M. 2014, PASA, 31, e040
Donnan, C. T., McLeod, D. J., Dunlop, J. S., et al. 2023, MNRAS, 518, 6011
Egami, E., Kneib, J. P., Rieke, G. H., et al. 2005, ApJ, 618, L5
Finkelstein, S. L., Papovich, C., Salmon, B., et al. 2012, ApJ, 756, 164
Franco, M., Akins, H. B., Casey, C. M., et al. 2023, arXiv:2308.00751
Fu, S., Jiang, L., Ning, Y., Liu, W., & Pan, Z. 2024, arXiv:2401.05920
Furtak, L. J., Shuntov, M., Atek, H., et al. 2023, MNRAS, 519, 3064
Gardner, J. P., Mather, J. C., Clampin, M., et al. 2006, SSRv, 123, 485
Greene, J. E., Labbe, I., Goulding, A. D., et al. 2023, arXiv:2309.05714
Gronke, M., Dijkstra, M., McCourt, M., & Oh, S. P. 2016, ApJL, 833, L26
Gupta, A., Jaiswar, R., Rodriguez-Gomez, V., et al. 2023, ApJL, 957, L35
Harikane, Y., Zhang, Y., Nakajima, K., et al. 2023, ApJ, 959, 39
Hayes, M., Scarlata, C., & Siana, B. 2011, Natur, 476, 304
Helton, J. M., Sun, F., Woodrum, C., et al. 2023, arXiv:2311.04270
Hoag, A., Treu, T., Pentericci, L., et al. 2019, MNRAS, 488, 706
Hu, E. M., Cowie, L. L., Barger, A. J., et al. 2010, ApJ, 725, 394
Huang, J. S., Zheng, X. Z., Rigopoulou, D., et al. 2011, ApJL, 742, L13
Iani, E., Caputi, K. I., Rinaldi, P., et al. 2023, arXiv:2309.08515
Infante, L., Zheng, W., Laporte, N., et al. 2015, ApJ, 815, 18

Jiang, L., Cohen, S. H., Windhorst, R. A., et al. 2020, ApJ, 889, 90
Jiang, L., Egami, E., Fan, X., et al. 2013a, ApJ, 773, 153
Jiang, L., Egami, E., Mechtley, M., et al. 2013b, ApJ, 772, 99
Jiang, L., Shen, Y., Bian, F., et al. 2017, ApJ, 846, 134
Juodžbalis, I., Conselice, C. J., Singh, M., et al. 2023, MNRAS, 525, 1353
Kartaltepe, J., Casey, C. M., Bagley, M., et al. 2021, COSMOS-Webb: The Webb Cosmic Origins Survey, JWST Proposal. Cycle 1, ID. # 1727
Kashikawa, N., Shimasaku, K., Malkan, M. A., et al. 2006, ApJ, 648, 7
Kashikawa, N., Shimasaku, K., Matsuda, Y., et al. 2011, ApJ, 734, 119
Labbé, I., Oesch, P. A., Bouwens, R. J., et al. 2013, ApJL, 777, L19
Langeroodi, D., & Hjorth, J. 2023, arXiv:2307.06336
Laporte, N., Pelló, R., Hayes, M., et al. 2012, A&A, 542, L31
Laporte, N., Streblyanska, A., Kim, S., et al. 2015, A&A, 575, A92
Lemaux, B. C., Fuller, S., Bradač, M., et al. 2021, MNRAS, 504, 3662
Li, Q., Conselice, C. J., Adams, N., et al. 2023, arXiv:2309.06932
Liu, Y., Dai, Y. S., Wuyts, S., Huang, J.-S., & Jiang, L. 2023, arXiv:2309.11559
Lyu, J., Alberts, S., Rieke, G. H., et al. 2023, arXiv:2310.12330
Madau, P. 1995, ApJ, 441, 18
Maiolino, R., Scholtz, J., Curtis-Lake, E., et al. 2023, arXiv:2308.01230
Maseda, M. V., Lewis, Z., Matthee, J., et al. 2023, ApJ, 956, 11
Mason, C. A., & Gronke, M. 2020, MNRAS, 499, 1395
Mateo, M., Bailey, J. I., Crane, J., et al. 2012, Proc. SPIE, 8446, 84464Y
Matthee, J., Naidu, R. P., Brammer, G., et al. 2023, arXiv:2306.05448
McLeod, D. J., McLure, R. J., & Dunlop, J. S. 2016, MNRAS, 459, 3812
Ning, Y., Cai, Z., Jiang, L., et al. 2023, ApJL, 944, L1
Ning, Y., Jiang, L., Zheng, Z.-Y., & Wu, J. 2022, ApJ, 926, 230
Ning, Y., Jiang, L., Zheng, Z.-Y., et al. 2020, ApJ, 903, 4
Oesch, P. A., Bouwens, R. J., Illingworth, G. D., et al. 2014, ApJ, 786, 108
Ono, Y., Ouchi, M., Harikane, Y., et al. 2018, PASJ, 70, S10
Ormerod, K., Conselice, C. J., Adams, N. J., et al. 2024, MNRAS, 527, 6110
Osterbrock, D. E., & Ferland, G. J. 2006, Astrophysics of Gaseous Nebulae and Active Galactic Nuclei (Sausalito, CA: Univ. Science)
Ouchi, M., Ellis, R., Ono, Y., et al. 2013, ApJ, 778, 102
Paulino-Afonso, A., Sobral, D., Ribeiro, B., et al. 2018, MNRAS, 476, 5479
Pearson, W. J., Wang, L., Alpaslan, M., et al. 2019, A&A, 631, A51
Peng, C. Y., Ho, L. C., Impey, C. D., & Rix, H.-W. 2002, AJ, 124, 266
Peng, C. Y., Ho, L. C., Impey, C. D., & Rix, H.-W. 2010, AJ, 139, 2097
Popping, G., Somerville, R. S., & Galametz, M. 2017, MNRAS, 471, 3152
Prieto-Lyon, G., Mason, C., Mascia, S., et al. 2023, ApJ, 956, 136
Rigby, J., Perrin, M., McElwain, M., et al. 2023, PASP, 135, 048001
Rinaldi, P., Caputi, K. I., Iani, E., et al. 2023, arXiv:2309.15671
Rinaldi, P., Caputi, K. I., van Mierlo, S. E., et al. 2022, ApJ, 930, 128
Rodriguez-Gomez, V., Genel, S., Vogelsberger, M., et al. 2015, MNRAS, 449, 49
Roy, N., Henry, A., Treu, T., et al. 2023, ApJL, 952, L14
Santini, P., Maiolino, R., Magnelli, B., et al. 2014, A&A, 562, A30
Saxena, A., Bunker, A. J., Jones, G. C., et al. 2023, arXiv:2306.04536
Schmidt, K. B., Treu, T., Bradač, M., et al. 2016, ApJ, 818, 38
Seeyave, L. T. C., Wilkins, S. M., Kuusisto, J. K., et al. 2023, MNRAS, 525, 2422
Shibuya, T., Ouchi, M., Nakajima, K., et al. 2014, ApJ, 785, 64
Simmonds, C., Tacchella, S., Maseda, M., et al. 2023, MNRAS, 523, 5468
Sobral, D., Matthee, J., Brammer, G., et al. 2019, MNRAS, 482, 2422
Sparre, M., Whittingham, J., Damle, M., et al. 2022, MNRAS, 509, 2720
Strait, V., Bradač, M., Coe, D., et al. 2020, ApJ, 888, 124
Tacconi, L. J., Genzel, R., & Sternberg, A. 2020, ARA&A, 58, 157
Tang, M., Stark, D. P., Chevallard, J., et al. 2021, MNRAS, 503, 4105
Taniguchi, Y., Murayama, T., Scoville, N. Z., et al. 2009, ApJ, 701, 915
Taylor, A. J., Barger, A. J., Cowie, L. L., Hu, E. M., & Songaila, A. 2020, ApJ, 895, 132
Tilvi, V., Pirzkal, N., Malhotra, S., et al. 2016, ApJL, 827, L14
Topping, M. W., Stark, D. P., Endsley, R., et al. 2022, ApJ, 941, 153
Treu, T., Roberts-Borsani, G., Bradac, M., et al. 2022, ApJ, 935, 110
Ventou, E., Contini, T., Bouché, N., et al. 2017, A&A, 608, A9
Whitler, L., Stark, D. P., Endsley, R., et al. 2023, MNRAS, 519, 5859
Williams, C. C., Alberts, S., Ji, Z., et al. 2023, arXiv:2311.07483
Wu, J., Jiang, L., & Ning, Y. 2020, ApJ, 891, 105
Yan, H., Finkelstein, S. L., Huang, K.-H., et al. 2012, ApJ, 761, 177
Zhang, H., Cai, Z., Liang, Y., et al. 2024, ApJ, 961, 63
Zhang, H., Ouchi, M., Itoh, R., et al. 2020, ApJ, 891, 177
Zheng, Z.-Y., Wang, J., Rhoads, J., et al. 2017, ApJL, 842, L22